

Sb–SnO₂ nanoparticles onto kaolinite rods: assembling process and interfacial investigation

Peiwei Hu · Huaming Yang

Received: 19 November 2011 / Accepted: 10 February 2012 / Published online: 25 February 2012
© Springer-Verlag 2012

Abstract In this article, we reported the synthesis of novel Sb–SnO₂/kaolinite (SK) nanocomposites by assembling antimony-doped tin oxide (ATO) nanoparticles on the surface of kaolinite rods without addition of dispersant. The samples were characterized by X-ray diffraction, transmission electron microscopy (TEM), high-resolution TEM, X-ray photoelectron spectroscopy (XPS), and N₂ adsorption–desorption techniques. The crystal size and loading density of ATO nanoparticles onto kaolinite rods could be controlled through the synthetic conditions. The color and resistivity of the composites varied with the loading density of ATO nanoparticles. Investigations of the interfacial binding between ATO layer and rod surface indicated that surface characteristics could facilitate the deposition of various metal oxides nanoparticles. XPS analysis demonstrated that the entrance of Sb⁵⁺ into SnO₂ crystallite led to the improvement of conductivity and the color change of the composites. The formation mechanism for SK composites was also discussed.

Keywords Kaolinite rods · Sb–SnO₂ nanoparticles · Coating · Composite structure · Interfacial investigation

Introduction

The compounding of the functional matrix and the silicate minerals can produce the advanced composites, and the main routes included the surface loading (Zhang et al. 2006; Aranda et al. 2008; Cao et al. 2008), porous assembly (Corma 1997; Stein et al. 2000; Gutiérrez et al. 2010), and intercalation technology (Pinnavaia 1983; Giannelis 1996; Krishnamoorti et al. 1996; Frost et al. 1998). Research achievements about the functional mineral-based composites have been successfully obtained in the fields of ecological environment (Ohashi et al. 2009), catalysis (Corma et al. 2010), optical (Wan et al. 2009; Bujdk et al. 2010), wave-absorbing materials (Mamedov et al. 2000; Blanco-Gutierrez et al. 2010), and energy storage (Chen et al. 2007). Antimony-doped tin oxide (ATO) is a well-known transparent semiconductor with a large band gap (>3.6 eV), providing transparency in the visible range and high n-type electric conductivity, which makes it a valuable alternative to the expensive indium tin oxide (ITO) (Mishra et al. 1995; Wang et al. 2009). The preparation of ATO nanoparticles with different shape, size, resistivity and degree of agglomeration has been addressed by different techniques (Zhang and Gao 2004; Posthumus et al. 2006; Li et al. 2010). Generally speaking, chemical methods provided much better controls over the particle size and their stability in solution than the physical methods. It is easy for the nanoparticles to form micron-sized secondary particles adhering to each other during the wet chemical synthesis. If that was the case, the properties of the as-synthesized samples would be affected by the size of the secondary particles. The sol–gel, polymeric precursor and co-precipitation techniques mostly provided either the large particles or the nanoparticle agglomerates, while the hydrothermal and solvothermal techniques were able to

P. Hu · H. Yang (✉)
School of Minerals Processing and Bioengineering,
Central South University, Changsha 410083, China
e-mail: hmyang@csu.edu.cn

P. Hu · H. Yang
Research Center for Mineral Materials, Central South
University, Changsha 410083, China

conveniently control the growth of ATO particles (Miller et al. 2009). The co-precipitation techniques highlighted the advantages in easily adjusting the preparing conditions as well as possessing the mass production capability among these methods, which makes it desirable for the large-scale production of ATO nanoparticles. Especially, uniform assembly of the ATO particles on the surface of special morphological minerals can effectively reduce the agglomeration degree of the nanoparticles and the preparation costs, and simultaneously improve its application performance. Many reports about this research focused on the silicate minerals such as mica (Tan et al. 2004; Sadeh et al. 2007), barite (Guffond et al. 2001; Hu et al. 2008), and montmorillonite (Boukerma et al. 2006).

Kaolinite ($\text{Al}_2\text{Si}_2\text{O}_5(\text{OH})_4$), a 1:1 dioctahedral aluminosilicate clay mineral, has two different basal cleavages faces, namely tetrahedral siloxane (Si–O–Si) surface and octahedral gibbsite (Al_2O_3) sheet. At the edges of kaolinite particles, octahedral alumina and silica tetrahedral sheets exposed reactive functional moieties, including aluminol (Al–OH) and silanol (Si–OH) groups (Murray 2000; Johnston et al. 2008; Turhan et al. 2010). For example, for one thing, coated with TiO_2 , flake-like kaolinite potentially improved the performance of air treatment technologies via enhancing adsorption and reactivity of target volatile organic compounds (VOCs) (Chong et al. 2009; Kibanova et al. 2009; Kocí et al. 2011); for another, TiO_2 -coated kaolin composite was used as a white pigment in view of enhancing pigmentary performance and reducing cost (Ninness et al. 2003; Lu et al. 2009). For the rod-like kaolinite, its physicochemical properties can be dramatically changed by surface modification with selected organic, inorganic, and biological species. Besides, this kind of functionalization will lead to the advanced properties.

In this article, we demonstrate a synthetic method to composite conductive materials with ATO nanoparticles uniformly assembled on the surface of the rod-like kaolinite without addition of dispersant. We also investigate the controllability of surface layer and the effects of assembled Sb–Sn compounds on the structure and property of the samples. The samples were characterized in detail by XRD, TEM, HRTEM, and XPS. In addition, a general synthesis mechanism is proposed.

Experimental

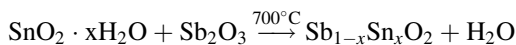
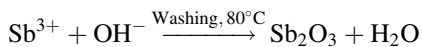
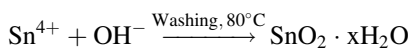
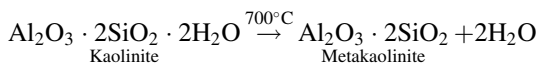
All of the chemicals, including stannic chloride hydrate ($\text{SnCl}_4 \cdot 5\text{H}_2\text{O}$), antimony trichloride (SbCl_3), hydrochloric acid (HCl), and ammonia liquor ($\text{NH}_3 \cdot \text{H}_2\text{O}$) were analytically pure and used without further treatment. A mixture acidic solution with initial $\text{Sb}^{3+}/\text{Sn}^{4+}$ salts molar

ratio of 0.16 dissolved in HCl (2.0 M) was prepared. In each experiment, a known quantity of rod-like kaolin (kaolinite content >95%) was dispersed in distilled water (total solids percent mass in volume, 10 wt%) at 60°C with constant stirring. The synthesis steps were carried out under simultaneously adding above mixture acidic solution and $\text{NH}_3 \cdot \text{H}_2\text{O}$ (30%), while the pH value of slurry was kept at 1.5 ± 0.1 . The composites with different Sn/Sb loading were obtained by adjusting the addition of mixture acidic solution. Then, stirring was continued for another 20 min and then maintained at a certain temperature for 1 h. The resultant precipitate was collected via filtering the solution, washed several times with distilled water to remove Cl^- , dried at 80°C for 4 h to produce a precursor. The precursor was calcined at 700°C for 1.5 h in air to finally form the conductive composites (SK). The Sn/Sb loading was designed as 2, 4, 8, 13, and 20%, and the corresponding conductive composites were marked as SK2, SK4, SK8, SK13, and SK20, respectively.

A powder X-ray diffractometer (RIGAKU D/max-2550 PC, Cu $k\alpha$ radiation, 40 kV, 300 mA) was used to identify the crystalline phase of the samples at a scanning rate of 2°/min over a range of 10–80° (2θ). The morphology and composite structure were carried out on a JEOL JEM 3010 transmission electron microscope (TEM), and energy-dispersive spectrometry (EDS) was performed with an EDAX X-ray energy-dispersive analysis system attached to the JEOL JEM 3010 TEM. The electrical structure and composition of the samples were analyzed by X-ray photoelectron spectroscopy (XPS) (Thermo ESCALAB 250, USA) measurements at room temperature. XPS spectra were recorded by using monochromatized Al $K\alpha$ radiation (1,486.6 eV) and the power was set to 150 W. The binding energy values were calibrated with reference to the C 1s peak (284.6 eV). The specific surface area (S_{BET}) of productions was calculated by the Brunauer–Emmet–Teller (BET) method. N_2 adsorption–desorption isotherms were obtained at 77 K using an ASAP 2020 unit. Prior to the adsorption experiment, the materials were vacuum-dried at 150°C for 6 h. About 1.5 g powder sample was putted into $\Phi 13$ mm model of stainless steel, pressed into slice with 10 MPa pressure. The universal meter DT890 was used for testing the ohmic resistance (Ω) of slice sample. The resistivity was calculated as: $\rho = RA/L$, where ρ was the resistivity of the sample (Ω cm), R the measured resistance (Ω), A the area of the sample pole (cm^2) and L the height of the sample pole (cm).

Results and discussion

The following reaction is suggested for the formation of conductive composites:



The theoretical mass of Sb–SnO₂/kaolinite composites was calculated according to above chemical equations. The initial quality of kaolin was 5 g, the mass ratio of SnCl₄ to kaolinite was 3:100, 6:100, 12:100, 20:100, and 30:100, respectively. The experimental mass of each composite was also well consistent with the calculated mass in terms of different Sn/Sb loading (Fig. 1), indicating the possibly complete coating of the initial Sn/Sb compounds on the rod surface. The color of the composites also became gradually darker with the increase of Sn/Sb loading (Fig. 1, inset).

The conductive properties of SK composites varied with the content of Sn/Sb loading (Fig. 2). Kaolinite was an excellent insulating material after heat treatment. When the Sn/Sb loading was 2 wt%, the volume resistivity of composites exceeded 10⁹ Ω cm. The volume resistivity decreased gradually with the increase in Sn/Sb loading and reached 7.8 × 10³ Ω cm at 20 wt% Sn/Sb compounds, indicating that much more surfaces would be coated with Sn/Sb compounds when the exposed surface areas of kaolinite reduced. Therefore, the composites performed the better conductivity.

Figure 3 illustrated the XRD patterns of metakaolin, SK2, SK4, SK8, SK13, and SK20 composites. The broad peak from 15 to 30° confirmed the amorphous structure of metakaolin from the calcination of kaolin at 700°C (Fig. 3a). Furthermore, the characteristic peak of

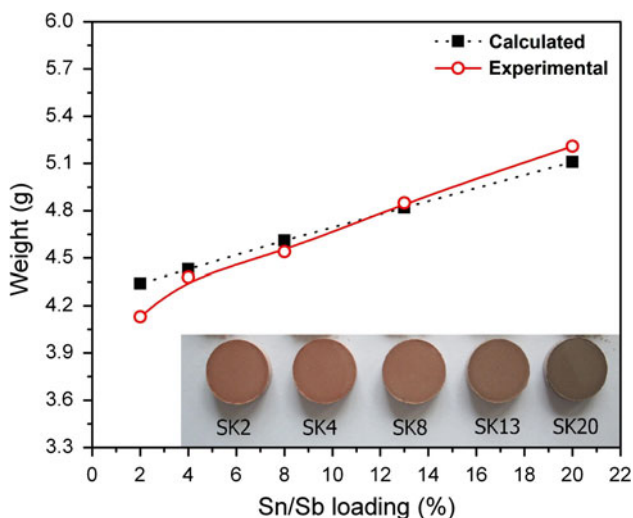


Fig. 1 Comparison of the calculated and experimental mass of SK with different Sn/Sb loading (the inset shows the photographs of the corresponding SK samples)

amorphous metakaolin was detected in all samples because of the lower content of SnO₂ nanoparticles. No other new phases were observed.

Samples with Sn/Sb less than 4 wt% did not show any obvious diffraction peaks of SnO₂, while three distinct diffraction peaks were observed at 26.5, 33.8, and 54.8° in SK samples with higher Sn/Sb loading of no less than 4

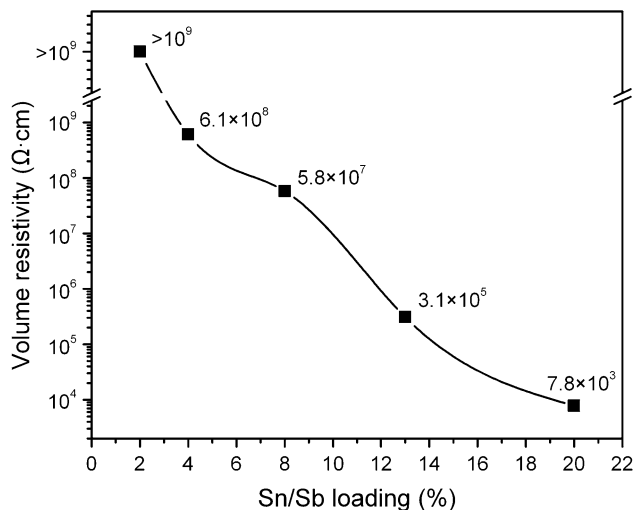


Fig. 2 Resistivities of SK samples with different Sn/Sb loading

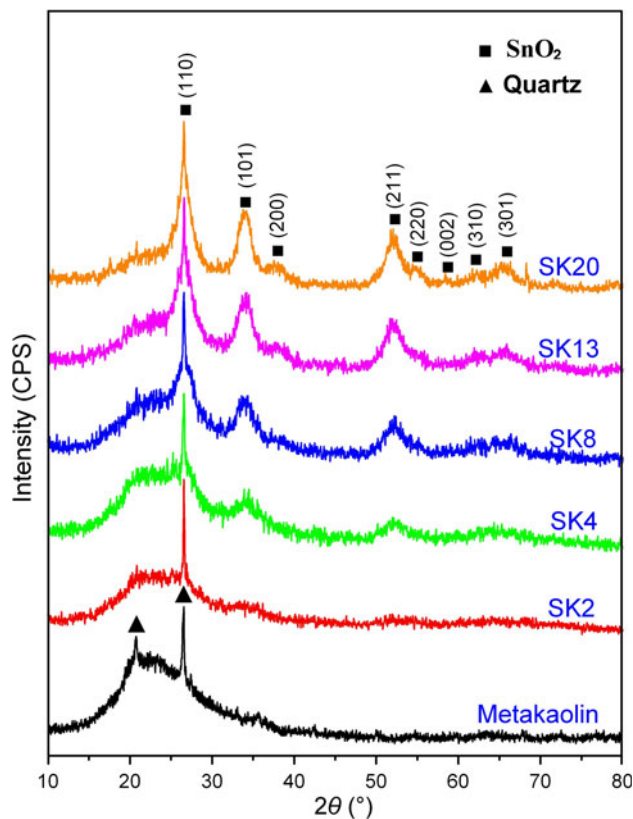
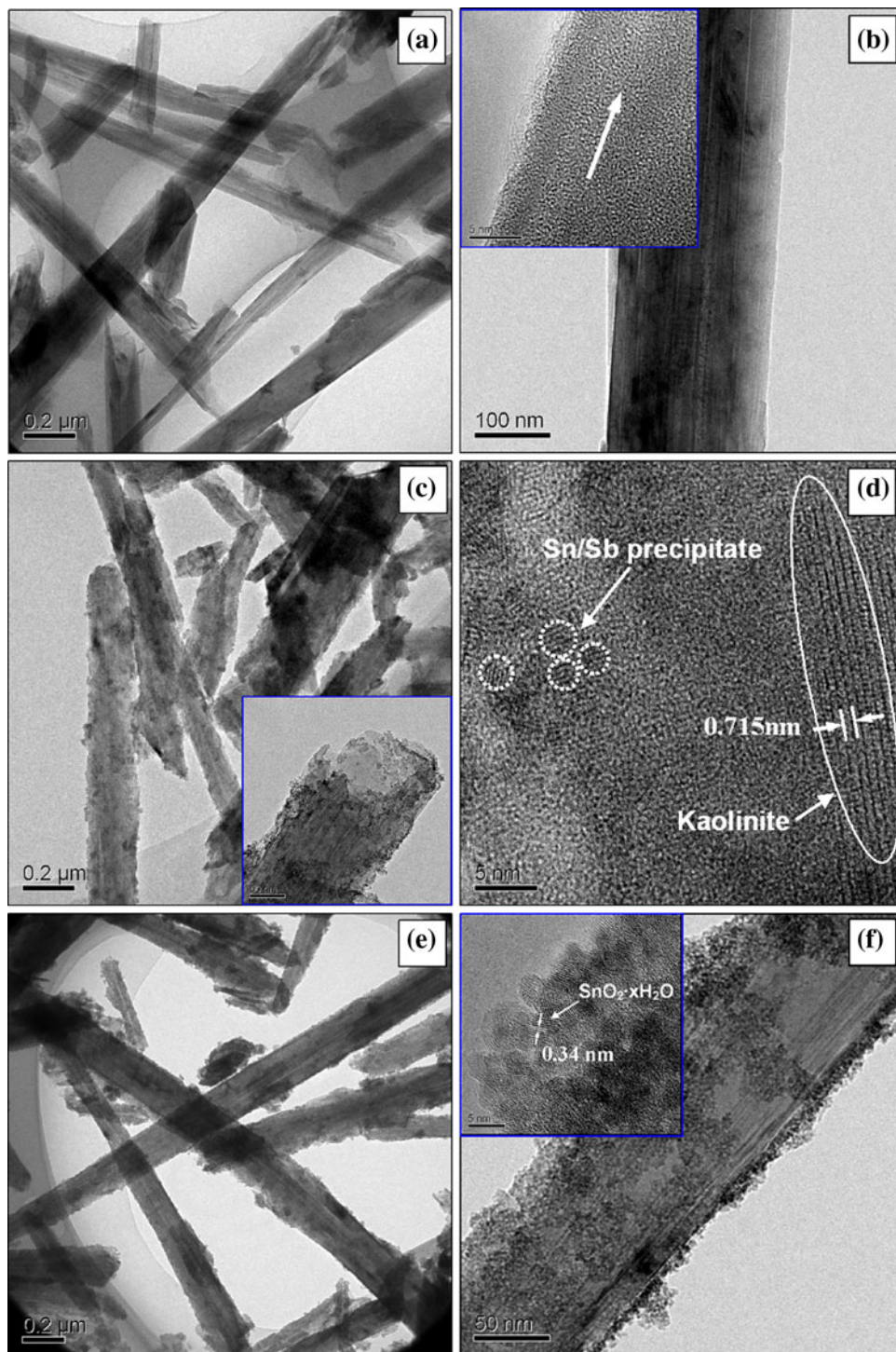


Fig. 3 XRD patterns of metakaolin and SK composites

Fig. 4 TEM images of kaolinite (a, b), precursor (SK4 before calcination) of SK4 (c, d) and precursor of SK13 (e, f)

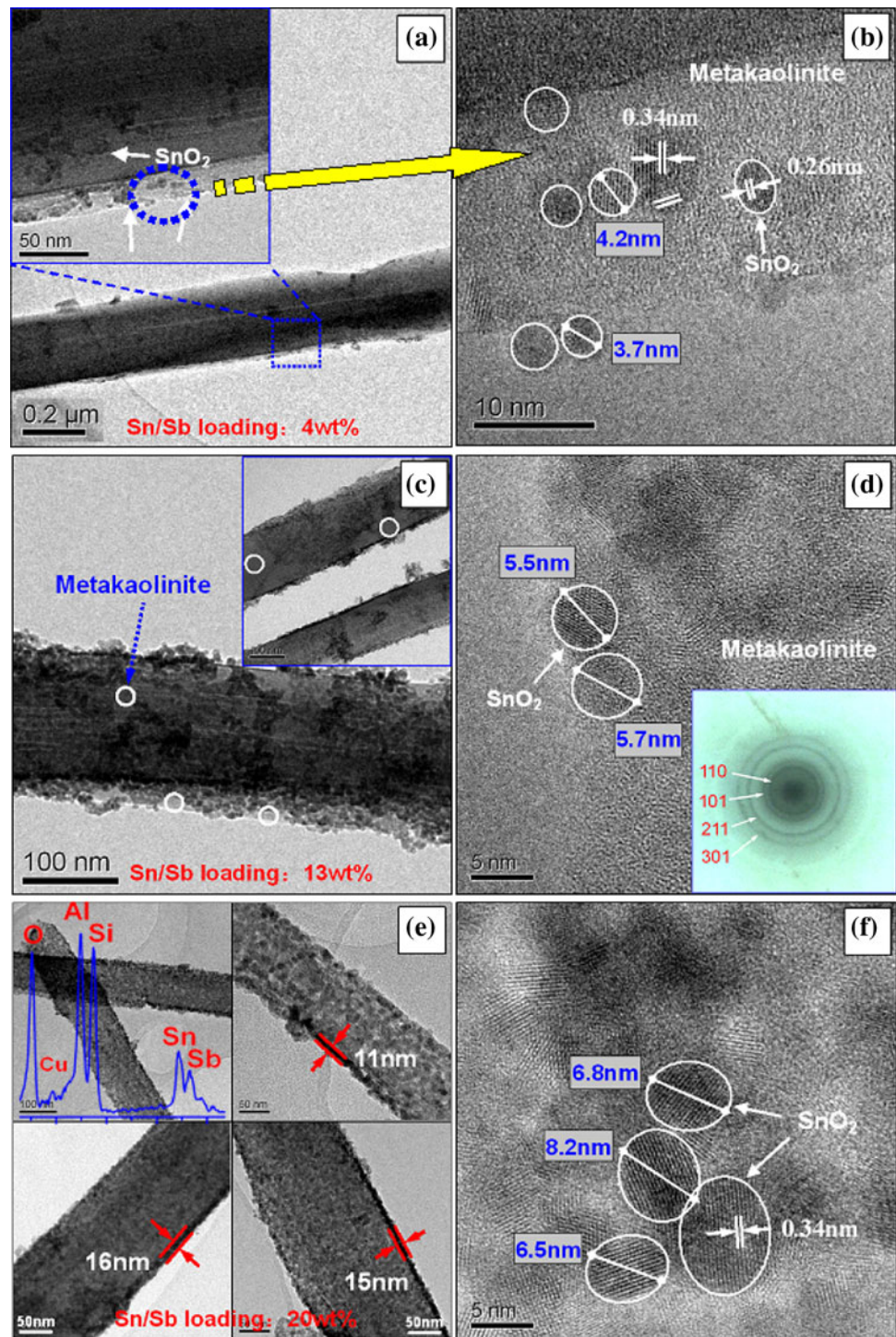


wt%, corresponding to the reflections of (110), (101), and (211) planes of SnO_2 tetragonal unit cell, respectively, which indicated the cassiterite structure (JCPDS no.41-1445) of SnO_2 in SK composites. On the other hand, the intensities of the above three peaks in SK20 were clearly enhanced and the peaks became more sharp than those of the other samples, mainly due to the increase in the content of Sn/Sb compounds. The increase in Sn/Sb loading (from

SK2 to SK20) could make the crystalline structure more integrated and increased the density of SnO_2 in the composites, but did not lead to the crystalline transformation of SnO_2 .

The effects of different Sn/Sb loading on the microstructure of the SK composites were further investigated. Kaolinite clay used here is a two-layered aluminosilicate with rod-like morphology in the submicrometer range, rod

Fig. 5 TEM and HRTEM images of SK4 (a, b), SK13 (c, d) and SK20 (e, f)



size of 100–200 nm in diameter and 1–5 μm in length. The rod showed an amorphous surface and obvious lengthways edge (Fig. 4a, b), possessing plenty surface hydroxyl groups. These extra hydroxyl groups are potential reaction sites for surface modification on the external surface (Yuan et al. 2008). Because surface edges and defects can bring higher specific surface energy and serve as nucleation sites

for metal oxide deposition, it was demonstrated that the surface with above characteristics could facilitate the deposition of various metal oxides nanoparticles through solution processes (Fang et al. 2008).

The formation of Sn/Sb compounds on the surface of kaolinite rods in precursor was confirmed by cross-section TEM observation. Figure 4c and e showed the morphology

of precursors with different Sn/Sb loading. A noticeable difference for the rods with or without loading lies in the surface roughness. Compared with original kaolinite rods (Fig. 4b), the Sn/Sb compounds on the rod surface was obvious (Fig. 4c, f). The (001) lattice fringes of kaolinite ($d = 0.715$ nm) and the (110) lattice fringes of SnO_2 ($d = 0.34$ nm) were clearly observed (Fig. 4d, f). The micrographs also indicated that the surface coverage became higher with the increase of the mass ratio of SnCl_4 to kaolinite. Much more nanoparticles were attached to the rod surfaces in the precursor of SK13 (Fig. 4f), we deduced that positively charged $\text{Sn}(\text{OH})_{4-n}^{n+}$ nanoparticles were first formed in the liquid and then adsorbed onto the kaolinite rods by electrostatic force. The newly formed particles were adsorbed by the exposed surface as the Sn/Sb loading increased, while previously adsorbed particles grew gradually. After the completion of the reaction and subsequent drying process, $\text{Sn}(\text{OH})_{4-n}^{n+}$ was transformed into $\text{SnO}_2 \cdot x\text{H}_2\text{O}$ nanoparticles attached onto the rod surfaces steadily.

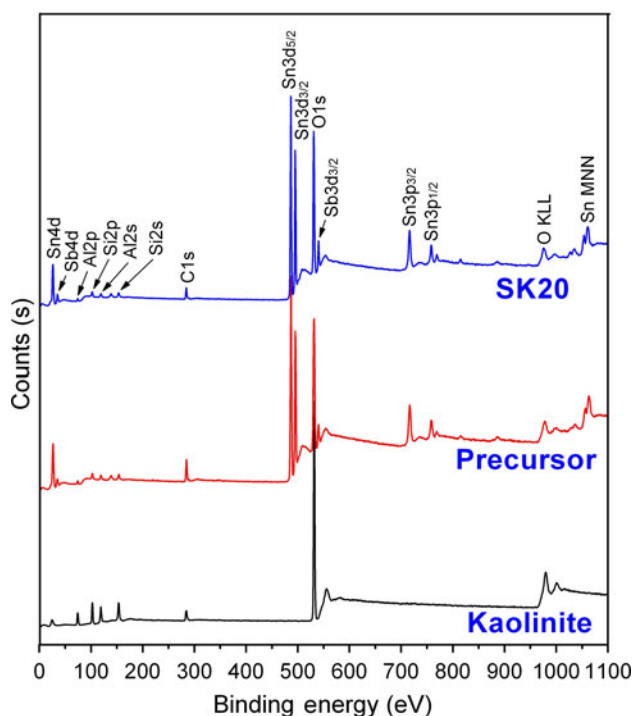


Fig. 6 XPS survey spectra of kaolinite, precursor and SK20

Table 1 Compositional analysis of samples from XPS studies

Samples	Atomic concentration/%					Concentration ratio	
	Al	Si	O	Sn	Sb	(Sn + Sb)/(Al + Si)	Sb/Sn
Kaolinite	10.9	13.3	75.8	0	0	0	–
Precursor	4.2	5.6	72.1	15.5	2.6	1.85	0.17
SK20	4.3	6.2	68.4	17.5	3.6	2.01	0.21

The surface coverage of nanoparticles on the surface of kaolinite rods was analyzed for the series of SK composites with different Sn/Sb loading. Compared with the corresponding precursor (Fig. 4), the ATO nanoparticles of SK composites contacted with each other more closely and tightly (Fig. 5). The morphology indicated that the number of ATO nanoparticles increased gradually as a consequence of Sn/Sb loading's increase (Fig. 5a, c, e), SK4 showed the uniform coating of ATO nanoparticles on the most of rod surfaces (Fig. 5c), but partial surface was not completely coated due to the inadequate Sn/Sb loading. As for the sample SK20 (Fig. 5e), the exterior surfaces of rods were fully coated with well-dispersed nanoparticles, and EDS analysis also confirmed the existence of O, Si, Al, Sn, and Sb elements in SK composites. The interplanar spacings of 0.34 and 0.26 nm corresponded to the (110) and (101) facets of the well-crystallized SnO_2 , respectively (Fig. 5b, f). The crystal size of SnO_2 varied with the Sn/Sb loading, but all in the range of 4–10 nm (Fig. 5b, d, f). The more the Sn/Sb compounds on the rod surface, the larger the crystal size of SnO_2 .

Full range XPS spectra of kaolinite, precursor, and SK20 were exhibited in Fig. 6. Compared with the original kaolinite, the peaks corresponding to Sn and Sb can be observed in both the precursor and SK20, further confirming the existence of elements Sn and Sb on the rod surface. The atomic composition, (Sn + Sb)/(Al + Si) ratio and Sb/Sn ratio were shown in Table 1. The Sb/Sn atomic ratios of precursor and SK20 were 0.17 and 0.21, respectively, near to the originally designed value of 0.16. Figure 7a and b exhibited the binding interface between Sn–Sb compounds and substrate rods for kaolinite and SK20, respectively. Clear interfaces were observed. The comparison of Al 2p and Si 2p peak positions for kaolinite, precursor and SK20 were also shown in Fig. 7c and d. There was obvious peak shift in binding energy (BE) position from original kaolinite, then precursor and finally to SK20 product, indicating the possible formation of Si–O–Sn and Al–O–Sn chemical bonds at the interfaces. Sn 3d_{3/2}–3d_{5/2} spin–orbit splitting energy of 8.4 eV was in well agreement with the previously reported value (Fig. 8a), their splitting Sn 3d_{5/2} spectra (Fig. 8b) exhibited three peaks at 486.2, 487.1, and 488.2 eV, assigned to Sn^{2+} , Sn^{4+} and Sn(–Cl) complex, respectively, the former two corresponded to SnO and SnO_2 , the latter may be

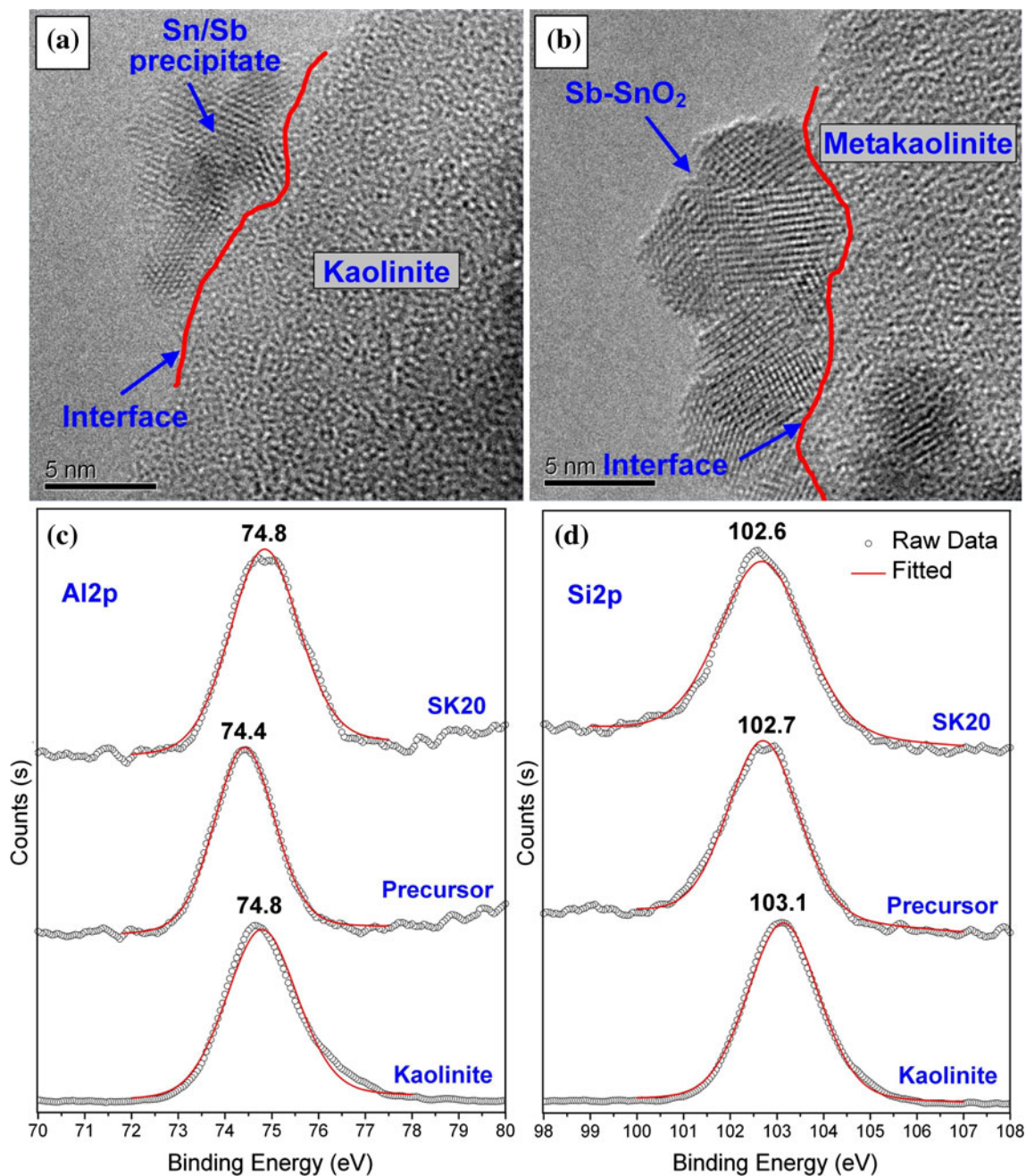


Fig. 7 HRTEM images of the interfaces between Sn/Sb compounds and substrate for **a** precursor and **b** SK20. The high-resolution XPS spectra of **c** Al 2p and **d** Si 2p for kaolinite, precursor, and SK20

resulted from the reaction between the Sn ions and Cl⁻ from the reaction environment (Li et al. 2006; Yang et al. 2010). After the precursor was calcined at 700°C, the Sn²⁺ and Sn(-Cl) peaks almost disappeared in SK20, the Sn⁴⁺ peak accounted for the majority.

High-resolution XPS analysis of the O 1s and Sb 3d peaks was further carried out to investigate the detailed information on the chemical states (Fig. 8c, d; Table 2). XPS spectra in the range of 527–544 eV for the precursor

and SK20 corresponded to the transitions of Sb and O atoms (Fig. 8c), but the Sb 3d5/2 transition was masked by the peak of O 1s transition, the Sb 3d5/2 peak was separated from the O 1s peak (Fig. 8d). The O 1s spectrum was decomposed into three contributions (Fig. 8c). The peak at BE of 531.0 eV was ascribed to the metal oxide (Sb–O) and the oxygen deficiency on the surface of SnO_{2-δ} crystallites (Batzill et al. 2005). The peak at 532.1 eV of O 1s was attributed to the Al–O and Si–O from the substrate and

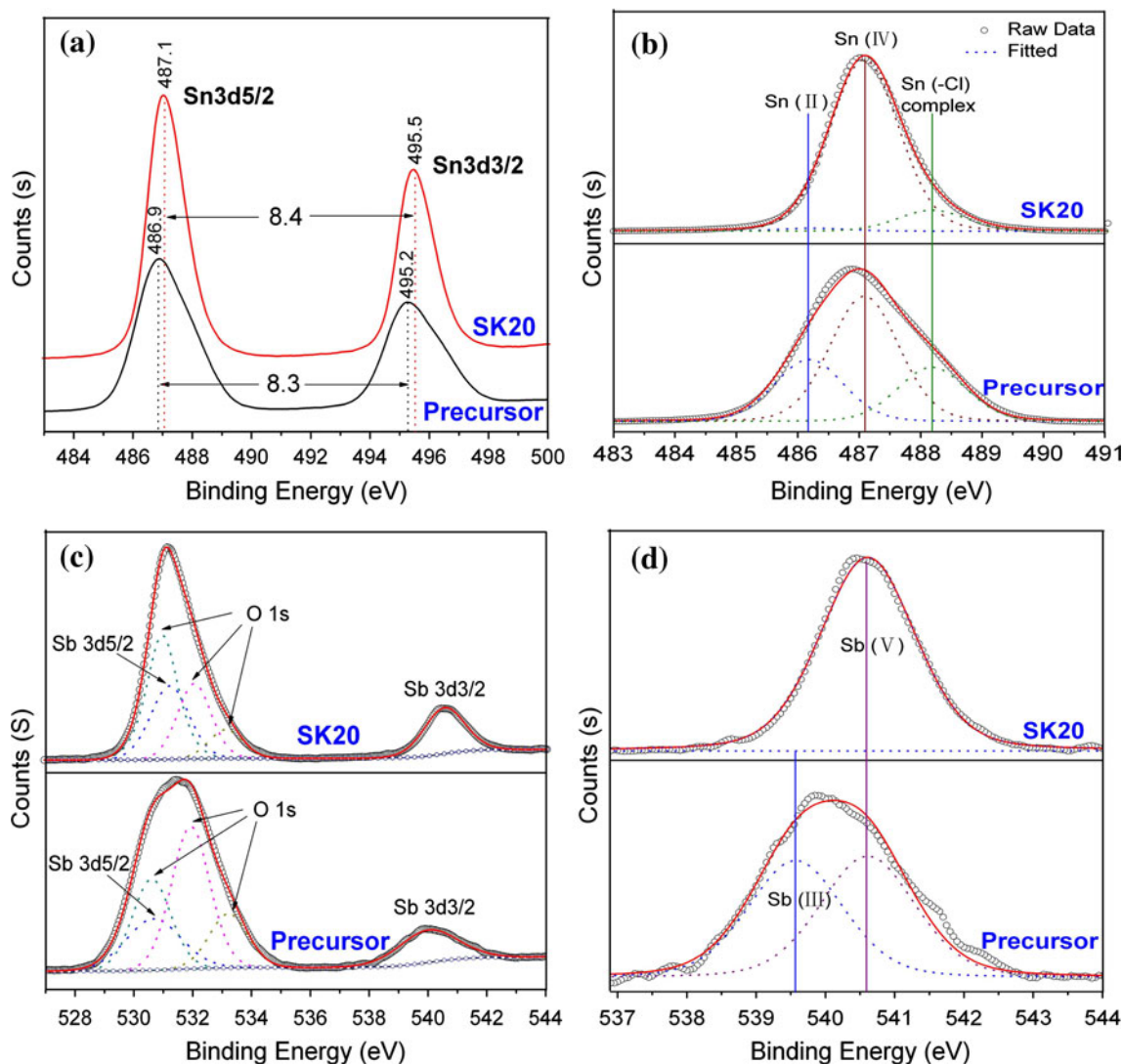


Fig. 8 High-resolution spectra of **a** Sn 3d, **b** Sn 3d_{5/2}, **c** O 1s and **d** Sb 3d_{3/2} transition region for precursor and SK20

the chemisorbed oxygen or hydroxyl ions such as O^- , O^{2-} or OH^- on the $SnO_{2-\delta}$ surface, the higher intensity of this peak in the precursor than that in SK20 indicated the existence of $SnO_2 \cdot xH_2O$ and hydroxyl from kaolinite. The peak around 533.1 eV was directly associated with H_2O on the surface (Montilla et al. 2004; Manesse et al. 2009; Yang et al. 2010).

The analysis of the surface Sb was restricted to the Sb 3d_{3/2} lines because of the overlap of the O 1s and Sb 3d_{5/2} lines, and Sb transition (3d_{3/2}) was employed to obtain the oxidation state of antimony. The XPS spectra of Sb 3d_{3/2} in precursor and SK20 provided precise information on the chemical state of Sb (Fig. 8d; Table 2). The Sb 3d_{3/2} spectrum had two characteristic peaks at 539.6 and 540.6 eV, identified as Sb^{3+} and Sb^{5+} , respectively (Marshall and Haverkamp 2010). The Sb^{5+} completely predominated in the SK sample, perfectly indicating the

complete oxidization of Sb in precursor into valence 5+ in SK. So, most of Sb^{5+} could enter the SnO_2 crystallite in SK, leading to the improvement of conductivity and the color change of the samples.

According to the above analysis, we suggest a possible formation mechanism for ATO/kaolinite composites. The deposition modes of ATO nanoparticles on the surface of kaolinite rods with different Sn/Sb loading were described in Fig. 9. The powdered kaolin, having the negatively charged surface, was well-dispersed in aqueous solution at pH of 1.5. After adding Sn/Sb mixed acid solution, the reaction reached a certain concentration of precipitation, and then generated a large number of positively charged sol particles, which was first adsorbed on the surfaces of kaolinite rods to form composite structure with the aid of the electrostatic attractions among them. As the amount of Sn/Sb mixed solution increased, part of the newly

Table 2 Distribution for the O 1s, Sn 3d5/2, and Sb 3d3/2 peaks

Samples	Precursor	SK20
Binding energy (eV)		
O 1s	531.6	531.1
Sn 3d5/2	486.9	487.1
Sb 3d3/2	540.0	540.6
O 1s region relative peak area (%)		
Metal–O (531.0 eV)	32	54
Al(Si)–O, –OH (532.1 eV)	50	34
–OH ₂ (533.1 eV)	28	12
Sn 3d5/2 relative peak area (%)		
Sn ²⁺ (486.2 eV)	26	2
Sn ⁴⁺ (487.1 eV)	52	88
Sn(–Cl) (488.2 eV)	22	10
Sb 3d3/2 relative peak area (%)		
Sb ³⁺ (539.6 eV)	49	0
Sb ⁵⁺ (540.6 eV)	51	100

The binding energy of O 1s in original kaolinite is 532.4 eV

formed sol particles were adsorbed on the exposed surface of the substrate, while another part made the original particles grow up. The coating process was finished until the substrate was covered downright, the number, particle size and coated density of ATO nanoparticles would be increased with the increase of Sn/Sb loading. The specific surface area (*S*_{BET}), pore volume of metakaolin and SK with different Sn/Sb loading were listed in Table 3, indicating that the surface area of SK4 with lower Sn/Sb loading (4 wt%) was slightly higher than that of uncovered substrate (metakaolin), while SK20 had the highest surface area of 30.4 m²/g. *S*_{BET} of samples steadily increased with the increase in Sn/Sb loading, which may be attributed to the increase of surface roughness resulted from the

Table 3 Specific surface area (*S*_{BET}) and pore volume for different samples

Samples	Sb–SnO ₂ (wt%)	<i>S</i> _{BET} (m ² /g)	Pore volume (cm ³ /g)
Metakaolin	0.0	17.4	0.08
SK4	4.0	21.3	0.09
SK8	8.0	23.7	0.09
SK20	20.0	30.4	0.09

deposition of ATO nanoparticles. No change in pore volume for all samples compared with metakaolin indicated that ATO layer onto kaolinite rods was dense without the formation of extra pores.

Conclusions

Novel conductive composites, with uniformly dispersed ATO nanoparticles on the surface of kaolinite rods, were successfully synthesized without the addition of any dispersant. The crystal size and surface coverage of ATO nanoparticles could be controlled via adjusting the reaction conditions. The surface edges and defects of rods served as nucleation sites and facilitated the deposition of various metal oxide nanoparticles via solution processes. Binding interface between ATO layer and rod surface demonstrated that surface characteristics facilitated the uniform assembly of nanosized oxides. Sb⁵⁺ entered into the SnO₂ crystallites, further led to the improvement of conductivity and the color change of the composites. Thus, our method could offer a more benign route to the general synthesis of mineral-based functional materials.

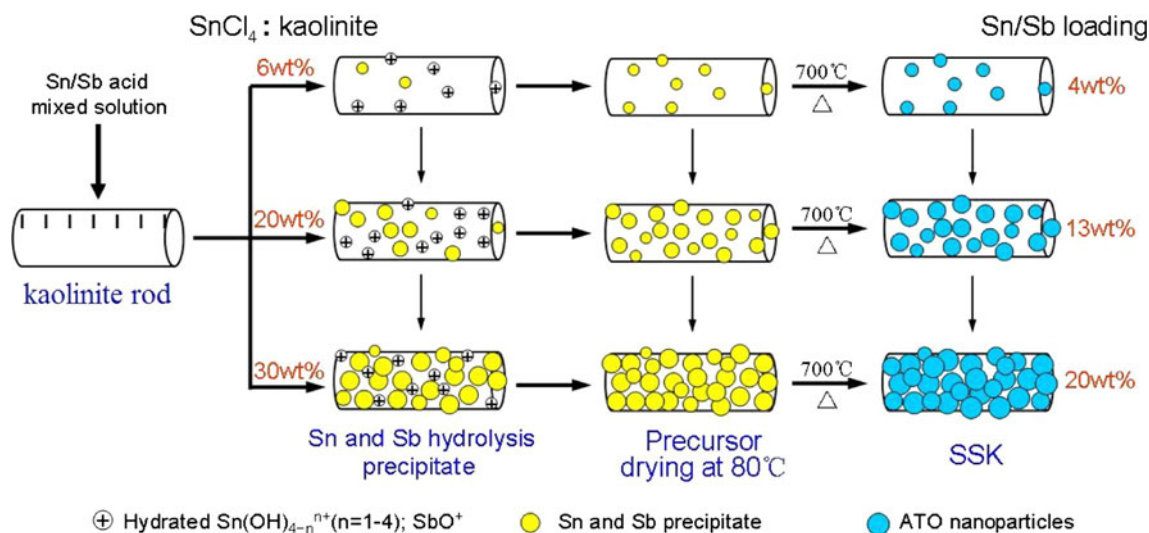


Fig. 9 Schematic for the formation process of SK composites

Acknowledgments This work was supported by the National Natural Science Foundation of China (50774095), the Scientific Research Foundation for ROCS of SEM (2011-1139), Hunan Provincial Innovation Foundation for Postgraduates (CX2010B042) and Excellent PhD Thesis Support Foundation of Central South University (2010ybfz056).

References

- Aranda P, Kun R, Martín-Luengo MA, Letaïef S, Dékány I, Ruiz-Hitzky E (2008) Titania-sepiolite nanocomposites prepared by a surfactant templating colloidal route. *Chem Mater* 20:84–91
- Batzill M, Katsiev K, Burst JM, Diebold U (2005) Gas-phase-dependent properties of SnO₂ (110), (100), and (101) single-crystal surfaces: structure, composition, and electronic properties. *Phys Rev B* 72:165414–165420
- Blanco-Gutierrez V, Urones-Garrote E, Torralvo-Fernandez MJ, Sez-Puche R (2010) ZnFe₂O₄ nanoparticles: different magnetic behavior when they are hosted in porous structures. *Chem Mater* 22:6130–6137
- Boukerma K, Piquemal J-Y, Chehimi MM, Mravčáková M, Omasová M, Beaunier P (2006) Synthesis and interfacial properties of montmorillonite/polypyrrole nanocomposites. *Polymer* 47:569–576
- Bujdk J, Chorvát D Jr, Iyi N (2010) Resonance energy transfer between rhodamine molecules adsorbed on layered silicate particles. *J Phys Chem C* 114:1246–1252
- Cao JL, Shao GS, Wang Y, Liu YP, Yuan ZY (2008) CuO catalysts supported on attapulgite clay for low-temperature CO oxidation. *Catal Commun* 9:2555–2559
- Chen L, Singh RK, Webley P (2007) Synthesis, characterization and hydrogen storage properties of microporous carbons templated by cation exchanged forms of zeolite Y with propylene and butylene as carbon precursors. *Microporous Mesoporous Mater* 102:159–170
- Chong MN, Vimonses V, Lei SM, Jin B, Chow C, Saint C (2009) Synthesis and characterisation of novel titania impregnated kaolinite nano-photocatalyst. *Microporous Mesoporous Mater* 117:233–242
- Corma A (1997) From microporous to mesoporous molecular sieve materials and their use in catalysis. *Chem Rev* 97:2373–2420
- Corma A, Daz U, Garca T, Sastre G, Verty A (2010) Multifunctional hybrid organic-inorganic catalytic materials with a hierarchical system of well-defined micro- and mesopores. *J Am Chem Soc* 132:15011–15021
- Fang HT, Sun X, Qian LH, Wang DW, Li F, Chu Y, Wang FP, Cheng HM (2008) Synthesis of tin (II or IV) oxide coated multiwall carbon nanotubes with controlled morphology. *J Phys Chem C* 112:5790–5794
- Frost RL, Klopogge JT, Tran THT, Kristof J (1998) The effect of pressure on the intercalation of an ordered kaolinite. *Am Mineral* 83:1182–1187
- Giannelis EP (1996) Polymer layered silicate nanocomposites. *Adv Mater* 8:29–35
- Guffond MC, Hunter RJ, Beattie JK (2001) Electroacoustic properties of barium sulfate particles coated with a conductive layer of antimony/tin(IV) oxides. *Chem Mater* 13:2619–2625
- Gutiérrez M, Escudey M, Escrig J, Denardin JC, Altbir D, Fabris JD, Cavalcante LCD, García-González MT (2010) Preparation and characterization of magnetic composites based on a nature zeolite. *Clays Clay Miner* 58:589–595
- Hu YH, Zhang HH, Yang HM (2008) Synthesis and electrical property of antimony-doped tin oxide powders with barite matrix. *J Alloys Compd* 453:292–297
- Johnston CT, Kogel JE, Bish DL, Kogure T, Murray HH (2008) Low-temperature FTIR study of kaolin-group minerals. *Clays Clay Miner* 56:470–480
- Kibanova D, Cervini-Silva J, Destaillets H (2009) Efficiency of clay-TiO₂ nanocomposites on the photocatalytic elimination of a model hydrophobic air pollutant. *Environ Sci Technol* 43:1500–1506
- Kočí K, Matějka V, Kovář P, Lacný Z, Obalová L (2011) Comparison of the pure TiO₂ and kaolinite/TiO₂ composite as catalyst for CO₂ photocatalytic reduction. *Catal Today* 161:105–109
- Krishnamoorti R, Vaia RA, Giannelis EP (1996) Structure and dynamics of polymer-layered silicate nanocomposites. *Chem Mater* 8:1728–1734
- Li Y, Zhao GY, Zhang WH, Chen YQ (2006) Fine pattern fabrication on SnO₂/Sb thin films formed by the sol-gel process. *Surf Interface Anal* 38:1291–1295
- Li YQ, Wang JL, Fu SY, Mei SG, Zhang JM, Yong K (2010) Facile synthesis of antimony-doped tin oxide nanoparticles by a polymer-pyrolysis method. *Mater Res Bull* 45:677–681
- Lu ZZ, Ren M, Yin HB, Wang AL, Ge C, Zhang YS, Yu LB, Jiang TS (2009) Preparation of nanosized anatase TiO₂-coated kaolin composites and their pigmentary properties. *Powder Technol* 196:122–125
- Mamedov A, Ostrander J, Aliev F, Kotov NA (2000) Stratified assemblies of magnetite nanoparticles and montmorillonite prepared by the layer-by-layer assembly. *Langmuir* 16:3941–3949
- Manesse M, Sanjines R, Stambouli V, Jorel C, Pelissier B, Pisarek M, Boukherroub R, Szunerits S (2009) Preparation and characterization of silver substrates coated with antimony-doped SnO₂ thin films for surface plasmon resonance studies. *Langmuir* 25:8036–8041
- Marshall AT, Haverkamp RG (2010) Electrocatalytic activity of IrO₂-RuO₂ supported on Sb-doped SnO₂ nanoparticles. *Electrochim Acta* 55:1978–1984
- Mishra KC, Johnson KH, Schmidt PC (1995) Electronic structure of antimony-doped tin oxide. *Phys Rev B* 51:13972–13976
- Miller V, Rasp M, Tefani G, Ba JH, Gnther S, Rathousky J, Niederberger M, Fattakhova-Rohlfing D (2009) Highly conducting nanosized monodispersed antimony-doped tin oxide particles synthesized via nonaqueous sol-gel procedure. *Chem Mater* 21:5229–5236
- Montilla F, Morallon E, Battisti AD, Barison S, Daolio S, Vazquez JL (2004) Preparation and characterization of antimony-doped tin dioxide electrodes. 3. XPS and SIMS characterization. *J Phys Chem B* 108:15976–15981
- Murray HH (2000) Traditional and new applications for kaolin, smectite, and palygorskite: a general overview. *Appl Clay Sci* 17:207–221
- Ninness BJ, Bousfield DW, Tripp CP (2003) Formation of a thin TiO₂ layer on the surfaces of silica and kaolin pigments through atomic layer deposition. *Colloids Surf A Physicochem Eng Asp* 214:195–204
- Ohashi F, Ueda S, Taguri T, Kawachi S, Abe H (2009) Antimicrobial activity and thermostability of silver 6-benzylaminopurine montmorillonite. *Appl Clay Sci* 46:296–299
- Pinnavaia TJ (1983) Intercalated clay catalysts. *Science* 220:365–371
- Posthumus W, Laven J, Gde With, van der Linde R (2006) Control of the electrical conductivity of composites of antimony doped tin oxide (ATO) nanoparticles and acrylate by grafting of 3-methacryloxypropyltrimethoxysilane (MPS). *J Colloid Interf Sci* 304:394–401
- Sadeh A, Sladkevich S, Gelman F, Prihodchenko P, Baumberg I, Berezin O, Lev O (2007) Sol-gel-derived composite antimony-doped, tin oxide-coated clay-silicate semitransparent and conductive electrodes. *Anal Chem* 79:5188–5195

- Stein A, Melde BJ, Schroden RC (2000) Hybrid inorganic–organic mesoporous silicates-nanoscope reactors coming of age. *Adv Mater* 12:1403–1419
- Tan JR, Shen LZ, Fu XS, Hou WX, Chen XZ (2004) Preparation and conductive mechanism of mica titania conductive pigment. *Dyes Pigment* 62:107–114
- Turhan Y, Dogan M, Alkan M (2010) Poly(vinyl chloride)/kaolinite nanocomposites: characterization and thermal and optical properties. *Ind Eng Chem Res* 49:1503–1513
- Wan CY, Li M, Bai X, Zhang Y (2009) Synthesis and characterization of photoluminescent Eu(III) coordination halloysite nanotube-based nanohybrids. *J Phys Chem C* 113:16238–16246
- Wang YD, Brezesinski T, Antonietti M, Smarsly B (2009) Ordered mesoporous Sb-, Nb-, and Ta-doped SnO₂ thin films with adjustable doping levels and high electrical conductivity. *ACS Nano* 3:1373–1378
- Yang D-J, Kamienczyk I, Youn DY, Rothschild A, Kim I-D (2010) Ultrasensitive and highly selective gas sensors based on electrospun SnO₂ nanofibers modified by Pd loading. *Adv Funct Mater* 20:4258–4264
- Yuan P, Southon PD, Liu ZW, Green MER, Hook JM, Antill SJ, Keper CJ (2008) Functionalization of halloysite clay nanotubes by grafting with γ -aminopropyltriethoxysilane. *J Phys Chem C* 112:15742–15751
- Zhang JR, Gao L (2004) Synthesis and characterization of antimony-doped tin oxide (ATO) nanoparticles. *Inorg Chem Commun* 7:91–93
- Zhang WD, Phang IY, Liu TX (2006) Growth of carbon nanotubes on clay: unique nanostructured filler for high-performance polymer nanocomposites. *Adv Mater* 18:73–77